

A Pathway to Sub-meV Detection of the Dark Universe: Robust Electron Avalanche in the PN junction at 10 mK

Aiqin Gao, Yiming Guo, Hengyu Wang, Xilei Sun, Xuegang Li, Junhua Wang, Junguang Lv, Guopu Qu, Lei Cao,

arXiv:2509.11954v3 [physics.ins-det] 20 Jan 2026

Abstract—The search for light dark matter and cosmic primordial neutrinos necessitates detectors with sub-millielectronvolt (sub-meV) energy thresholds. While superconducting quantum sensors have approached this sensitivity, they often face significant challenges regarding readout complexity and scalability. To address these limitations, we propose a hybrid Superconductor-Insulator-P-N (S-I-P-N) detector architecture. This concept combines the high sensitivity of superconducting Cooper pair breaking with the massive intrinsic gain of semiconductor electron avalanches. A critical prerequisite for this scheme is operation at millikelvin (mK) temperatures, raising the critical fundamental question of whether silicon PN junctions can sustain avalanche multiplication in a regime where carrier freeze-out is severe. Here, we experimentally validate the critical semiconductor amplification stage of the proposed detector. We demonstrate that Silicon Photomultipliers (SiPMs) retain robust Geiger-mode avalanche capabilities at 10 mK. We report a single-photoelectron gain of order 10^6 and a dark count rate as low as 5 mHz/mm², 7 orders of magnitude lower than at room temperature. These results confirm the viability of high-gain semiconductor readout in the deep cryogenic regime, clearing the primary obstacle regarding the semiconductor component for the realization of scalable, sub-meV threshold S-I-P-N detectors.

Index Terms—Dark matter, Silicon Photomultipliers (SiPMs), Millikelvin (mK) temperatures, Electron avalanche, Gain, Dark count rate (DCR), Sub-meV detection, S-I-P-N detector.

I. INTRODUCTION

This work was supported by the State Key Laboratory of Particle Detection and Electronics (Grant No. E429T1TD1D) and the National Key Research and Development Program (Grant No. 2022YFB3503600).

Co-first author: Aiqin Gao, is with School of Nuclear Science and Technology, University of South China, Hengyang 421001, China (e-mail: gao2653211091@gmail.com).

Co-first author: Yiming Guo, is with University of Chinese Academy of Sciences, Beijing 100049, China (e-mail: phys.yimingguo@gmail.com).

Hengyu Wang, is with University of Chinese Academy of Sciences, Beijing 100049, China (e-mail: wanghengyu@ihep.ac.cn).

Junguang Lv, is with Institute of High Energy Physics, Chinese Academy of Sciences, Beijing 100049, China (e-mail: lujg@ihep.ac.cn).

Junhua Wang, is with Beijing Key Laboratory of Fault-Tolerant Quantum Computing, Beijing Academy of Quantum Information Sciences, Beijing 100193, China (e-mail: wangjh@baqis.ac.cn).

Lei Cao, is with School of Science, Sun Yat-sen University, Shenzhen 518107, Guangdong, China. (e-mail: caolei7@mail2.sysu.edu.cn).

Guopu Qu, is with School of Nuclear Science and Technology, University of South China, Hengyang 421001, China (e-mail: quguopu@usc.edu.cn).

Corresponding author: Xilei Sun, is with Institute of High Energy Physics, Chinese Academy of Sciences, Beijing 100049, China (e-mail: sunxl@ihep.ac.cn).

Corresponding author: Xuegang Li, is with Beijing Key Laboratory of Fault-Tolerant Quantum Computing, Beijing Academy of Quantum Information Sciences, Beijing 100193, China (e-mail: lixg@baqis.ac.cn).

THE Standard Model of particle physics, despite its immense success, describes only about 5% of the energy content of the universe [1]. The remaining 95% resides in the “dark sector,” composed of Dark Energy and Dark Matter (DM). Astrophysical observations, from galaxy rotation curves to the cosmic microwave background, provide compelling gravitational evidence for DM, yet its particle nature remains elusive. While traditional searches have focused on Weakly Interacting Massive Particles (WIMPs) in the GeV–TeV mass range, the null results from decades of experiments have shifted the paradigm toward Light Dark Matter (LDM) candidates (keV–GeV range) [2]. Simultaneously, cosmology predicts the existence of the Cosmic Neutrino Background (C ν B) [3], a relic from the Big Bang similar to the Cosmic Microwave Background (CMB). Unlike high-energy neutrinos from stars or reactors, these primordial neutrinos have cooled to ultra-low kinetic energies (approximately ~ 0.1 meV) due to the expansion of the universe.

Unveiling the nature of LDM and directly detecting the C ν B remain two of the most pressing challenges in fundamental physics. However, the physical properties of these “ghostly” particles impose severe constraints on detection technology. Due to their light mass and low velocity, the energy transferred during an interaction with a detector is minute. For instance, the capture of a relic neutrino or the scattering of an LDM particle typically deposits energy in the sub-millielectronvolt (sub-meV) regime. This lies far below the threshold of traditional scintillation and ionization detectors, which are fundamentally limited to the eV scale by the bandgap or ionization energy of materials [4]. Consequently, addressing these frontiers requires a new generation of quantum sensors capable of bridging this six-order-of-magnitude energy gap [5].

Superconducting detectors, such as Transition-Edge Sensors (TES) [6] and Superconducting Nanowire Single-Photon Detectors (SNSPD) [7], represent a major leap in sensitivity. Yet, they have generally plateaued at the sub-electron volt (sub-eV) range [8], falling short of the meV targets. More recently, detectors based on superconducting quantum technologies have emerged, achieving sensitivities approaching the meV threshold. Typical examples include Quantum Parity Detectors (QPD) [9], [10] and Quantum Capacitance Detectors (QCD) [11], [12]. These devices utilize the coherent states of superconducting qubits or single Cooper-pair boxes to detect the breaking of individual Cooper pairs with exquisite precision. However, despite their impressive sensitivity, they face significant challenges in practical application. QPD and QCD

technologies typically rely on complex microwave readout schemes and are highly sensitive to environmental coherence, making the multiplexing and scaling required for large-mass dark matter searches technically demanding.

To bridge this gap between ultra-low threshold sensitivity and scalable readout, we propose the S-I-P-N architecture, as illustrated in Fig. 1. In this design, incident particles break Cooper pairs with minute binding energy [13] in a superconducting absorber. The resulting quasiparticles then tunnel through an insulating barrier (Al_2O_3) into a semiconductor PN junction, where they are accelerated by a strong electric field to trigger an electron avalanche (Geiger mode). This process effectively converts a single quantum event into a macroscopic current pulse. Unlike QPD or TES systems, this design elegantly bypasses the complexity of quantum readouts by shifting the amplification burden to the semiconductor. This unique hybrid approach combines the sub-meV sensitivity of superconductors with the robust, macroscopic readout of classical detectors, thereby solving the scalability issue that currently limits quantum sensing arrays.

However, the feasibility of this concept hinges on a critical uncertainty: the behavior of silicon junctions at mK temperatures. At ~ 10 mK, severe carrier freeze-out threatens to stifle the avalanche process by eliminating free carriers and altering electric field distributions [14], [15]. Verifying whether silicon can sustain stable Geiger-mode discharges in this “frozen” state is therefore the pivot point for the entire S-I-P-N technology.

In this work, we experimentally validate the semiconductor amplification stage of the proposed detector. We utilize commercial Silicon Photomultipliers (SiPMs)—arrays of single-photon avalanche diodes—as a proxy to investigate the avalanche dynamics of silicon at 10 mK. The SiPM is a novel semiconductor photodetector and has experienced rapid advancement in recent decades. It consists of an array of multiple Geiger-mode avalanche photodiode pixels connected in parallel, each composed of an avalanche photodiode in series with a quenching resistor, enabling single-photon detection capability [16], [17]. SiPMs offer high gain ($>10^6$), fast response, compact size, low operating voltage (tens of volts), high detection efficiency, strong resistance to magnetic fields, and robustness against saturation and aging [18]–[20]. These features have led to widespread applications in high-energy physics, nuclear medicine, and laser detection [19]–[21].

We present a characterization of key performance parameters, including breakdown voltage, gain, photon resolution capability, and dark count rate, in a dilution refrigerator environment. Our results demonstrate that silicon devices retain robust avalanche capabilities with excellent signal-to-noise ratios at 10 mK, thereby removing the primary obstacle for the realization of the S-I-P-N detector and establishing a solid foundation for future hybrid quantum sensing technologies.

II. EXPERIMENTAL SETUP AND DATA ACQUISITION SYSTEM

A. Cryogenic platform and thermal coupling

As shown in Fig. 2(a), the experiments were conducted in a Bluefors XLD1000sl dilution refrigerator measurement

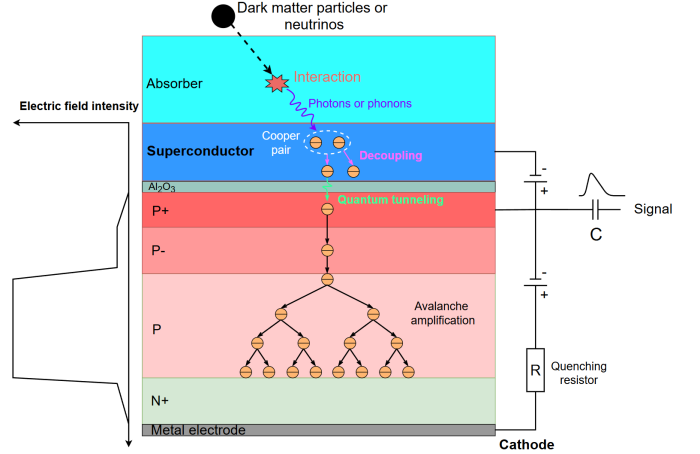


Fig. 1. Schematic diagram of S-I-P-N detector concept. A superconductor (planned to use Al) is grown on a highly doped p-type semiconductor via ultrathin epitaxial techniques. When quasiparticles in the Al film encounter the heavily doped semiconductor interface, they rapidly recombine with free electrons/holes there, converting all their energy into useless phonons. To enable efficient quasiparticle injection, a 2 nm-thick Al_2O_3 thin insulating layer (which can be formed by natural oxidation at room temperature or precisely controlled by atomic layer deposition, ALD) is inserted between the Al and the p^+ layer, forming a tunnel contact with moderate contact resistance (non-ohmic contact with resistance in the $\text{k}\Omega$ to $\text{M}\Omega$ range). This structure combined with the PN junction forms an S-I-P-N configuration (I denotes the thin insulating layer). The PN junction uses a traditional avalanche diode design, consisting, from top to bottom, of a heavily doped p^+ region, a lightly doped p^- region, a moderately doped p region, and a heavily doped n^- region. Particles to be detected (e.g., dark matter particles or neutrinos) interact with the sensitive material causing energy deposition. This deposited energy is transferred in the form of phonons or photons to the superconductor, which breaks Cooper pairs into quasiparticles. Since the superconductor is very thin and the interface is a tunnel contact, these quasiparticles can efficiently tunnel into the p^+ region. Under the strong electric field of the PN junction, avalanche multiplication occurs, producing an observable signal. A quenching resistor is connected in series in the circuit to implement passive quenching, rapidly terminating the avalanche.

system [22], capable of reaching a base temperature of 8~10 mK with a cooling power of $30\sim 34 \mu\text{W}$ at 20 mK. To minimize thermal load, a commercial SiPM (OnSemi J-series 60035, $6\times 6 \text{ mm}^2$) was selected for its low breakdown voltage characteristics [23]. The SiPM circuit board (Fig. 2(c)) was securely mounted on the Mixing Chamber (MXC) flange using gold-plated copper screws. A thin layer of thermal grease was applied between the board and the flange to maximize thermal conductivity.

To ensure the SiPM junction reached thermal equilibrium with the refrigerator base, the temperature of the MXC flange was monitored by a Ruthenium Oxide (RuOx) sensor (Bluefors R30184), calibrated against a noise thermometer with an uncertainty of ± 0.5 mK below 50 mK. After the MXC flange reached the base temperature, the system was maintained in this state for over 72 hours prior to data acquisition to allow for complete thermalization of the SiPM assembly. During the entire measurement period, the temperature was actively monitored, achieving a stability better than ± 0.5 mK (peak-to-peak deviation). Given the robust thermal contact and the long equilibrium time, we consider the SiPM device temperature to be effectively thermalized to 10 mK.

B. Optical setup and shielding

Due to the solidification of conventional optical coupling agents at cryogenic temperatures, a “dry” coupling method was employed. A plastic scintillator (Fig. 2(b)), dimensioned to match the SiPM sensitive area ($6 \times 6 \text{ mm}^2$) and wrapped in Enhanced Specular Reflector (ESR) film, was placed in direct contact with the SiPM surface without optical grease. An ^{241}Am α/γ source ($\approx 10^4 \text{ Bq}$) was positioned to irradiate the scintillator, serving as a stable pulsed light source. To suppress environmental electromagnetic interference and thermal radiation, a multi-stage shielding strategy was implemented. The SiPM assembly was wrapped in tinfoil, and the dilution refrigerator was enclosed within three layers of copper, two layers of aluminum alloy, and one layer of permalloy+aluminum composite shielding buckets. The entire system was operated within an ultra-high vacuum chamber.

C. Readout electronics and data acquisition

The electrical readout scheme is also illustrated in Fig. 2(a). A Keithley 6517B electrometer provided a stable, low-noise reverse bias voltage to the SiPM and monitored the DC leakage current (IV characteristics). The fast transient current signals from the SiPM were transmitted via coaxial cables to room-temperature electronics. These signals were converted to voltage and amplified by a high-speed transimpedance preamplifier based on the LMH6629 chip [24] (as shown in Fig. 2(d)), powered by a RIGOL DP831A DC supply providing an output of $\pm 2.5 \text{ V}$. The detailed circuit diagram of the preamplifier is described in Ref. [25]. Waveforms were digitized and recorded using a Tektronix MSO64B oscilloscope (1 GHz bandwidth, 50 GS/s sampling rate) or a CAEN DT5751 digitizer for offline analysis. Data processing, including baseline subtraction, waveform integration, and peak fitting, aims to extract gain, breakdown voltage, and so on.

III. EXPERIMENTAL METHODS AND RESULTS

A. Breakdown voltage and operating voltage range

The accurate determination of the breakdown voltage (V_{bd}) is a prerequisite for reliable SiPM operation. The breakdown voltage is defined as the minimum bias voltage required to trigger avalanche multiplication in a SiPM. Above the breakdown voltage, electron-hole pairs acquire sufficient energy to initiate the avalanche process, resulting in high gain and observable electrical signals. Determining the breakdown voltage at cryogenic temperatures is complex due to changes in semiconductor physics. We evaluated the breakdown voltage using two distinct methodologies:

1) Gain-Intercept Method (Gain-breakdown voltage, V_{Gbd}):

First, we employed the Gain-Intercept Method to determine the Gain-breakdown voltage. This method relies on the linear relationship between SiPM gain and bias voltage (V_{bias}) in the Geiger mode. By plotting the measured Gain versus V_{bias} and performing a linear fit, the breakdown voltage V_{Gbd} is defined as the x-intercept (the voltage where Gain extrapolates to zero) [25].

The Gain of the SiPM is defined as the number of carriers generated during a single avalanche discharge, and can be given by [26]:

$$\text{Gain} = \frac{C_d + C_q}{q_e} \cdot V_{\text{ov}} = \frac{Q_{\text{SPE}}}{q_e} \quad (1)$$

where C_d and C_q is the junction and parasitic capacitances, $q_e = 1.602 \times 10^{-19} \text{ C}$ is the elementary charge, $V_{\text{ov}} = V_{\text{bias}} - V_{\text{bd}}$ is the overvoltage, Q_{SPE} is the mean charge generated by a single avalanche from a single photoelectron (SPE).

In our experimental setup, the current signal from the SiPM (I_{in}) is converted into a voltage signal (V_{out}) by a transimpedance preamplifier (based on the LMH6629 chip). The relationship is governed by the transimpedance gain (Z_{TIA}) and the load resistance ($R_{\text{load}} = 50 \Omega$), and can be given by:

$$V_{\text{out}} = I_{\text{in}} \cdot R_f = I_{\text{in}} \cdot Z_{\text{TIA}} \cdot R_{\text{load}} \quad (2)$$

Where R_f is the feedback resistor, and $Z_{\text{TIA}} = R_f/R_{\text{load}}$ is the normalized transimpedance gain (unitless).

The charge of a SPE event is calculated by integrating the output voltage waveform over a specific time window:

$$Q_{\text{SPE}} = \int I_{\text{in}} dt = \frac{\int V_{\text{out}}(t) dt}{Z_{\text{TIA}} \cdot R_{\text{load}}} \quad (3)$$

The charge integration spectrum measured at 10 mK is shown in Fig. 3(a). In the charge integration spectrum, the photoelectron peaks often deviate from a symmetric Gaussian shape and exhibit an asymmetric “tail”. This asymmetry is primarily attributed to afterpulsing, where trapped carriers are released during partial cell recovery, producing correlated pulses with fractional charge that add to the primary photoelectron signal. To extract the peak mean (μ) and standard deviation (σ) accurately, we fit the peaks using the Crystal Ball function [27], which stitches a Gaussian core to a power-law tail:

$$f(x; \alpha, n, \bar{x}, \sigma) = N \cdot \begin{cases} \exp\left(-\frac{(x-\bar{x})^2}{2\sigma^2}\right), & \text{for } \frac{x-\bar{x}}{\sigma} < \alpha \\ A \left(B + \frac{x-\bar{x}}{\sigma}\right)^{-n}, & \text{for } \frac{x-\bar{x}}{\sigma} \geq \alpha \end{cases} \quad (4)$$

Where \bar{x} and σ are the mean and width of the Gaussian core. α defines the transition point between the Gaussian and the power-law tail. n controls the slope of the tail. N is a normalization factor. A and B are constants ensuring continuity of the function and its first derivative.

Q_{SPE} can be obtained by dividing the distance between the mean values of the first photoelectron peak (μ_1 , 1 P.E.) and the second photoelectron peak (μ_2 , 2 P.E.) by the Z_{TIA} :

$$Q_{\text{SPE}} = \frac{\mu_2 - \mu_1}{Z_{\text{TIA}}} \quad (5)$$

The results extracted from the gain-versus-bias measurements shown in Fig. 3(b). The gain at 10 mK exhibits excellent linearity with bias voltage. By fitting the linear region ($R^2 = 0.99983$) and extrapolating to zero gain, we determined $V_{\text{Gbd}}^{10 \text{ mK}} = 21.08 \pm 0.20 \text{ V}$.

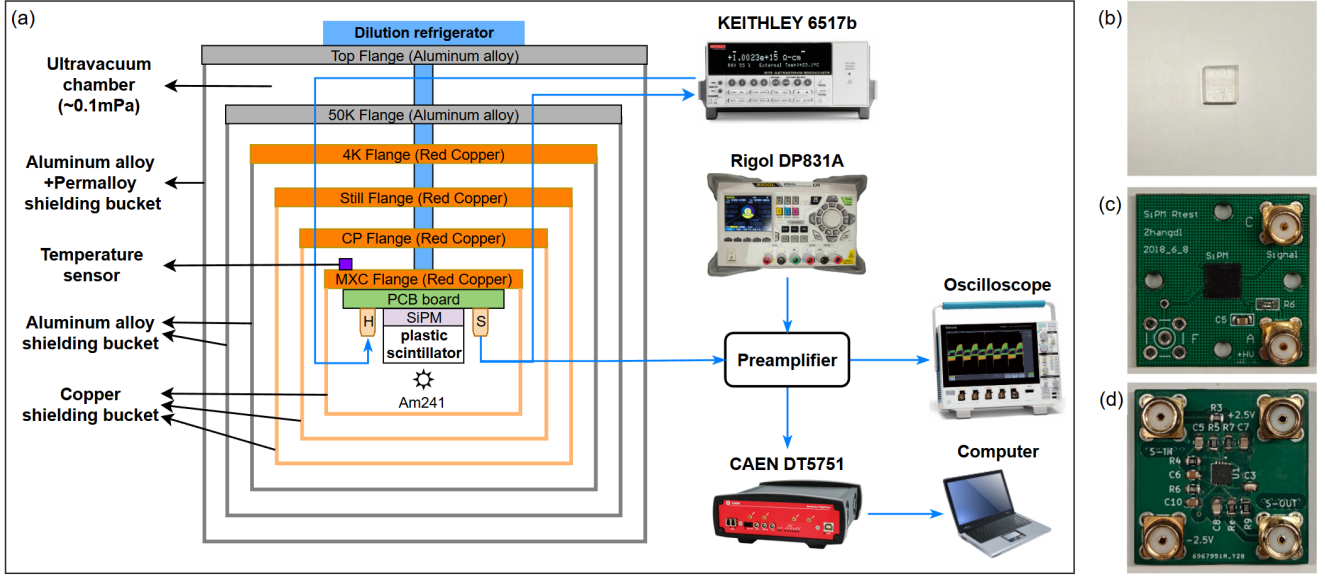


Fig. 2. (a) Schematic of the experimental setup inside the dilution refrigerator and the external readout, power, and data acquisition equipment. The SiPM assembly is secured with screws to the MXC flange maintained at 10 mK and is thermally coupled to it using thermal grease; the temperature is monitored by a calibrated RuOx sensor. A plastic scintillator, wrapped in ESR film and irradiated by a ^{241}Am α/γ source, is directly coupled to the SiPM and serves as a stable pulsed light source for characterization. The system is enclosed in multi-layer electromagnetic shielding to suppress external interference. The SiPM circuit board is connected to room-temperature power and readout electronics outside the refrigerator via two coaxial cables; (b) The photograph of the plastic scintillator, which has been cut to the same size as the SiPM, $6 \times 6 \text{ mm}^2$, and is used as a stable light source to characterize the performance of the SiPM; (c) The photograph of the SiPM circuit board, where the SiPM is soldered at the center of the circuit board; (d) The photograph of the preamplifier circuit board, a transimpedance amplifier based on the LMH6629 chip, used to convert the SiPM current signal into a voltage signal.

2) *IV-Inflection Method (Current-breakdown voltage, V_{Ibd}):* Second, we analyzed the IV-Inflection Method to get the Current-breakdown voltage, defined as the voltage corresponding to the maximum of the logarithmic derivative of the current, which is the inflection point of the reverse Current-Voltage (IV) characteristic, given by:

$$V_{\text{Ibd}} = \text{argmax}\left(\frac{d(\ln I)}{dV}\right) = \text{argmax}\left(\frac{1}{I} \frac{dI}{dV}\right) \quad (6)$$

At this point, the SiPM current increases rapidly. This is an empirical but widely accepted method for measuring breakdown voltage, not derived from a physical equation [28], [29].

As shown by the black curve in Fig. 3(c), the differential curve at 10 mK exhibits two distinct peaks. The first peak represents the avalanche breakdown (V_{Ibd}), while the second peak corresponds to the “second divergence” (V_{sd}). Second divergence is the divergence of the IV curve caused by self-sustaining avalanches resulting from excessively high correlated noise probability (dominated by afterpulse and enhanced by crosstalk) [30], [31]. We first smoothed the IV curve using a cubic spline interpolation, then differentiated it and fitted the result with a Landau–Gaussian convolution function to extract the peak positions.

The temperature dependence of V_{bd} is summarized in Fig. 3(d). A non-monotonic trend is observed: V_{bd} decreases from 100 K to 50 K, driven by the suppression of optical phonon scattering which extends the carrier mean free path [14]. However, an anomalous increase appears from 50 K down to 10 mK. This phenomenon is a signature of carrier freeze-out, where the thermal ionization of dopants

becomes inefficient, necessitating a higher electric field to initiate impact ionization [15], [32].

The breakdown voltage of the SiPM is a unique physical parameter. In ideal conditions, both methods yield identical values, as there is no physical basis for distinct breakdown voltages. While consistent at room temperature, V_{Ibd} tends to overestimate the breakdown voltage at temperatures below 20 K due to the reduced photocurrent sensitivity and flattening of the IV curves. This overestimation effect becomes more pronounced as the temperature decreases. Consequently, V_{Gbd} is adopted as the standard definition for V_{bd} in this work.

3) *Operating voltage range:* Avalanche breakdown sets the lower limit of the operating voltage, while second divergence sets the upper limit. As shown by the red curve in Fig. 3(c), in the dark the SiPM’s IV curve does not show the avalanche breakdown because the dark current is too low, but the second divergence is clearly visible. In our measurements, we take the secondary divergence voltage corresponding to the IV curve in the dark environment as V_{sd} . Fig. 4 shows the dark noise signal of the SiPM during second divergence in a dark environment, where correlated noise has caused a self-sustaining avalanche, rendering the SiPM non-functional, and the generated heat can lead to refrigerator failure.

Based on these measurements, the stable operating range is defined as the interval between the breakdown voltage and the second divergence voltage ($V_{\text{bd}} < V_{\text{bias}} < V_{\text{sd}}$). As visualized in Fig. 5, the SiPM maintains a stable operating window of approximately 5 V (21.08 V \sim 26.27 V) at 10 mK, providing sufficient headroom for high-gain operation.

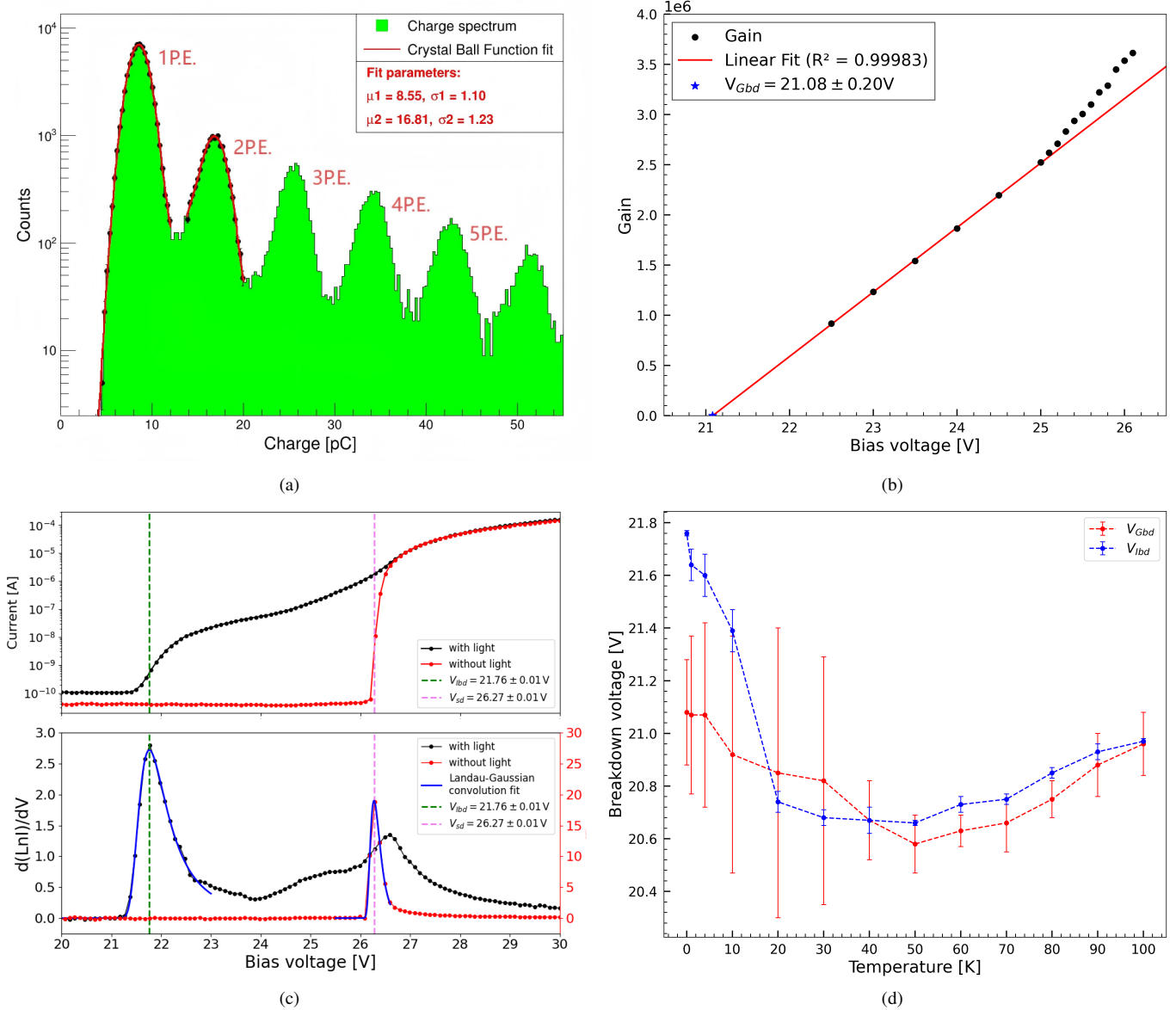


Fig. 3. (a) Charge integration spectrum obtained from plastic scintillation induced only by γ -rays from ^{241}Am ($V_{\text{bias}} = 23.5$ V). The first peak is the single-photoelectron (1.P.E.), the second is the double-photoelectron (2.P.E.), and so on. Peak positions and standard deviations were obtained by fitting with Crystal Ball functions. The Q_{SPE} is given by the difference between the first two peak positions divided by Z_{TIA} , i.e. $Q_{\text{SPE}} = (\mu_2 - \mu_1)/Z_{\text{TIA}}$; (b) SiPM gain versus bias voltage V_{bias} at 10 mK. The breakdown voltage is determined from the intercept of the fit curve with the x -axis. The gain deviates from linearity at high bias due to the imminent onset of secondary divergence; (c) The IV curve obtained at 10 mK from plastic scintillation induced by $\alpha + \gamma$ rays from ^{241}Am and the IV curve obtained in the dark environment (top) along with their derivatives (bottom). The curves have been spline-interpolated and differentiated; V_{Ibd} and V_{sd} are determined by fitting the extremum of $d(\ln I)/dV$. The secondary divergence voltage corresponding to the IV curve in the dark environment is taken as V_{sd} . (d) Temperature dependence of V_{Gbd} and V_{Ibd} from 100 K to 10 mK. The vertical error bars come from fit parameter uncertainties. Both methods yield the same trend: the breakdown voltages decrease from 100 K to 50 K and then increase from 50 K to 10 mK.

B. Signal response and performance

1) *Output waveform characteristics:* At cryogenic temperatures, the SiPM pulse signal underwent significant changes. We recorded the signal shapes at different temperatures ($V_{\text{ov}} = 2.5$ V), as shown in Fig. 6(a). The output waveform of a SiPM microcell is modeled by an equivalent circuit consisting of the diode depletion layer resistance (R_d), the junction capacitance (C_d), the quenching resistor (R_q), and parasitic capacitances (C_q) [26]. The waveform features a typical rapid rise component determined by the avalanche process and an exponential decay component determined by the recovery

time, can be given by [32]:

$$\tau_{\text{rise}} \propto R_d(C_d + C_q) \quad (7)$$

$$\tau_{\text{decay}} \propto R_q(C_d + C_q) \quad (8)$$

In our measurements at 10 mK, the rise time remains relatively constant, limited primarily by the preamplifier bandwidth.

As temperature decreases from 100 K to 50 K, the polysilicon quenching resistor R_q increases significantly, dominating the recovery process and leading to a longer decay time [33]. Upon further cooling from 50 K to 10 mK, carrier freeze-out

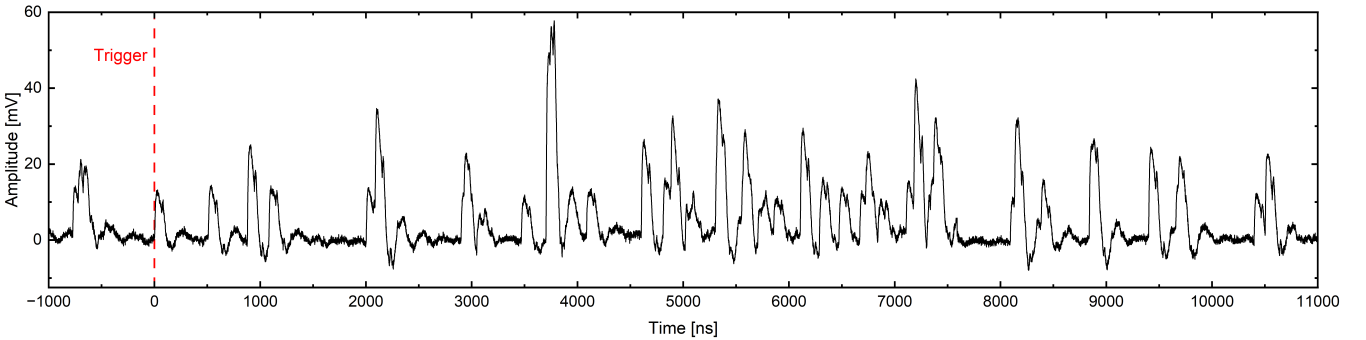


Fig. 4. Dark noise waveform of the SiPM during the second divergence in a dark environment ($V_{\text{bias}} = 26.3$ V). After the onset of the second divergence, crosstalk and afterpulses generate self-sustaining avalanches.

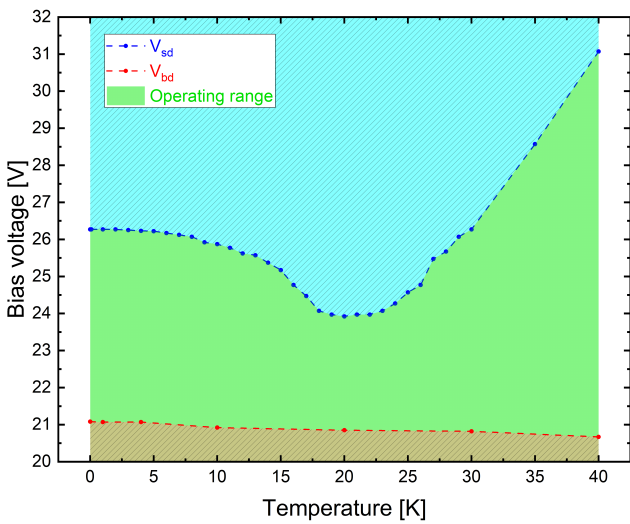


Fig. 5. The operating voltage range of the SiPM is ($V_{\text{bd}} < V_{\text{bias}} < V_{\text{sd}}$). If the voltage exceeds V_{sd} , the SiPM will not operate properly. In practice, the operating voltage should be kept well below the secondary divergence to avoid the failure of the refrigerator.

substantially reduces the effective doping concentration [32], causing the depletion width W_d to widen and the junction capacitance $C_d = A\epsilon_{Si}/W_d$ (where A is the effective junction area of a single microcell, ϵ_{Si} is the permittivity of silicon, and W_d is the depletion width) to decrease sharply. This capacitance reduction becomes the dominant factor in the time constant, reversing the trend and shortening the decay time below 50 K, with the decay time seeming to reach its minimum around 10 mK.

A faster decay can enhance the detection efficiency but can also lead to the generation of high-frequency signal components. Due to impedance mismatches in the long coaxial cables used in the dilution refrigerator, these signals may reflect, causing the ringing and overshoot observed in the waveforms.

2) *Gain variation:* According to the previous formula Eq. 1, gain is positively correlated with junction capacitance (C_d), and a decrease in temperature will inevitably lead to a decrease in gain due to the reduction in C_d . Waveform broadening and distortion at cryogenic temperatures affects

gain calculations. To ensure complete charge collection of pulses at all temperatures, we select sufficiently wide and fixed integration windows for each temperature based on the measured pulse durations. Fig. 6(c) shows the gain as a function of overvoltage. At 10 mK, the gain remains on the order of 10^6 and scales linearly with V_{ov} , although it is reduced by a factor of ~ 4.44 compared to room temperature due to the decrease in junction capacitance.

3) *Photon resolution capability:* The distortion of waveforms and the decrease in gain at cryogenic temperatures may worsen the photon resolution capability of the SiPM [37]. Fig. 6(d) shows the integral charge spectrum at different temperatures. At 10 mK, the SiPM's photon resolution capability does decrease, but it can still distinguish between varying numbers of photons. The distinct separation of discrete photoelectron peaks (1 P.E., 2 P.E., etc.) confirms the quantized nature of the avalanche process in the deep cryogenic regime. We fitted the first photoelectron peak with a Crystal Ball function to evaluate the SPE resolution (R_{SPE}), calculated using :

$$R_{\text{SPE}} = \frac{\text{FWHM}}{\mu} = \frac{2.355 \cdot \sigma}{\mu} \quad (9)$$

Fig. 6(d) shows the SPE resolution as a function of overvoltage. At 10 mK, the SPE resolution is clearly worse than at other temperatures. However, since it can still distinguish between different numbers of photons, this remains acceptable. At $V_{\text{ov}} = 2.5$ V, the SPE resolution is approximately 30%. In the future, we will design readout circuits specifically optimized for low-temperature environments, which are expected to significantly improve photon resolution.

C. Noise characterization

1) *Dark count rate:* Under dark conditions, due to thermal excitation or tunneling effects, SiPMs spontaneously generate electron-hole pairs, which undergo avalanche multiplication in the strong electric field within the depletion region, leading to dark counts. The dark count rate (DCR) is influenced by the sensitive area, V_{ov} , and temperature [34]. The DCR decreases from 50 kHz/mm² at room temperature [23] to 0.1 Hz/mm² at liquid nitrogen temperature (77 K) [35] when $V_{\text{ov}} = 2.5$ V.

In SiPMs, the presence of optical crosstalk (direct and delayed) and afterpulses, along with their cascading effects,

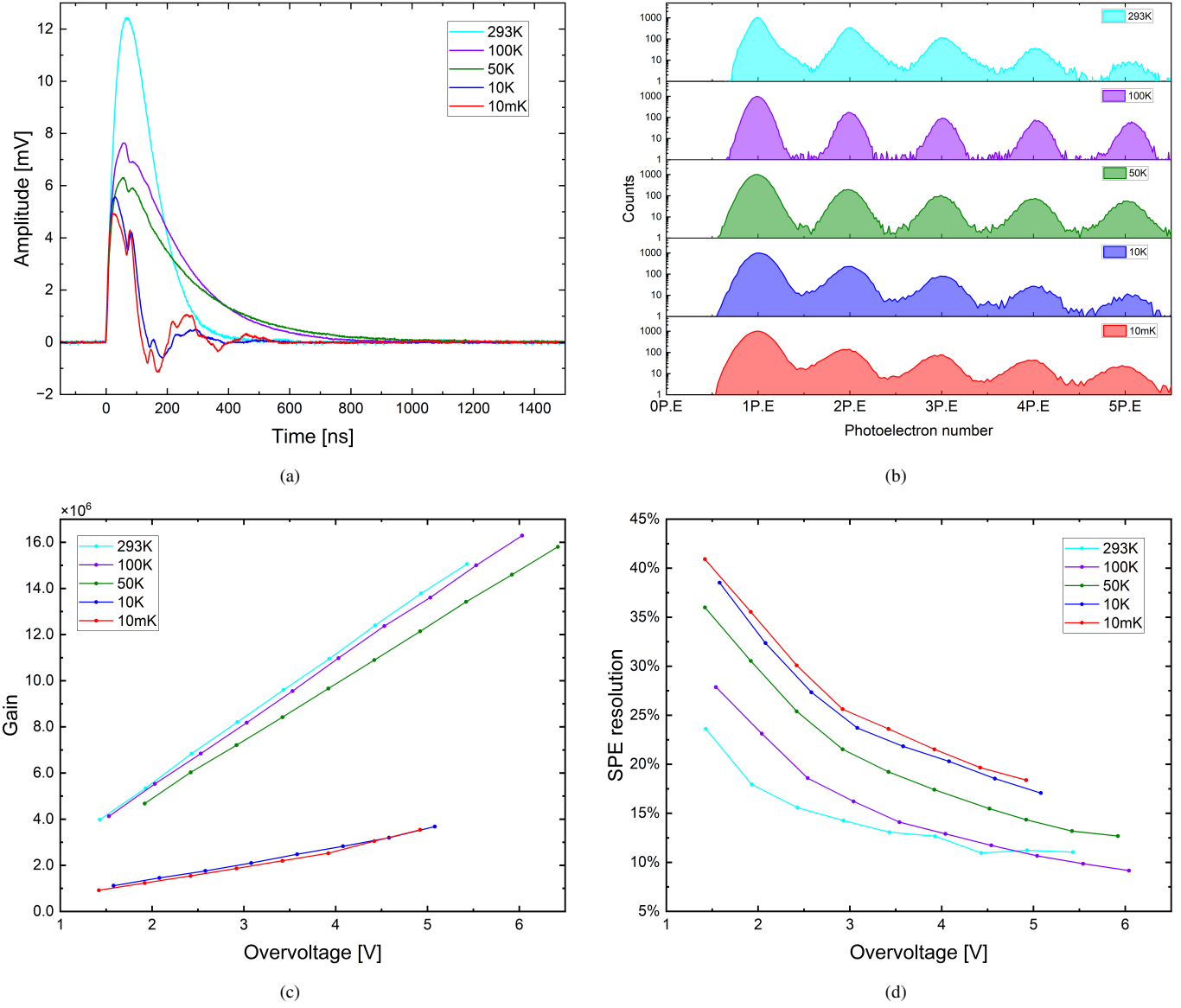


Fig. 6. (a) Average pulse waveforms at different temperatures ($V_{ov} = 2.5$ V). As the temperature decreases, the output amplitude of the SiPM continuously decreases. The rise time of the SiPM shows almost no change. The decay time gradually increases from room temperature to 50 K due to the increase in quenching resistance R_q ; however, when the temperature decreases from 50 K to 10 mK, the decay time decreases sharply, following the rapid reduction of the junction capacitance C_d , and seems to reach a minimum at 10 mK. The ringing and overshoot of the signal are due to impedance mismatches in the coaxial cables used; (b) Integral charge spectrum of single-photoelectron (SPE) at different temperatures ($V_{ov} = 2.5$ V). At 10 mK, the photon resolution indeed worsens, but it can still distinguish between different numbers of photons; (c) Gain as a function of overvoltage at different temperatures. At 10 mK, the gain is reduced by a factor of 4.44 compared to room temperature due to the decrease in junction capacitance; (d) SPE resolution as a function of overvoltage at different temperatures. Due to the reduced gain and waveform distortion, the single-photon resolution of the SiPM exhibits a certain degree of degradation.

causes the measured dark count rate (Total DCR) to include contributions from these correlated noises, making it higher than the true primary dark count rate (Primary DCR). To exclude the effects of delayed crosstalk and afterpulses, we adopt a self-veto window of 10 μ s measurement method (since almost all delayed crosstalk and afterpulses occur within 10 μ s after the primary trigger) to eliminate false triggers [34]. Although this method can remove spurious events, it also leads to the loss of real primary signals, as shown in Fig. 7. Fortunately, this counting loss can be statistically corrected using :

$$N_{\text{measured}} = \frac{N_{\text{real}}}{T} \cdot (T - N_{\text{measured}} \cdot T_{\text{Hold-off}}) \quad (10)$$

Where N_{measured} is the number of dark counts recorded by the oscilloscope in Holdoff mode over a specific time period, N_{real} is the actual number of dark counts of the SiPM during the same period, $T_{\text{Hold-off}}$ is the hold-off time (10^{-5} s), and T is the total elapsed time (from the start to the stop of acquisition). After rearranging Eq. 10, N_{real} can be expressed as :

$$N_{\text{real}} = \frac{N_{\text{measured}}}{1 - \frac{N_{\text{measured}} \cdot T_{\text{Hold-off}}}{T}} = \frac{N_{\text{measured}} \cdot T}{T - N_{\text{measured}} \cdot T_{\text{Hold-off}}} \quad (11)$$

The statistical uncertainty of the measured count follows Poisson statistics :

$$\delta N_{\text{measured}} = \sqrt{N_{\text{measured}}} \quad (12)$$

The uncertainty on the dead-time-corrected primary count N_{real} is obtained by standard error propagation :

$$\delta N_{\text{real}} = \frac{\sqrt{N_{\text{measured}}}}{\left(1 - \frac{N_{\text{measured}} \cdot T_{\text{Hold-off}}}{T}\right)^2} = \sqrt{N_{\text{measured}}} \cdot \left(\frac{N_{\text{real}}}{N_{\text{measured}}}\right)^2 \quad (13)$$

Fig. 8(b) shows the DCR as a function of overvoltage at 10 mK. Due to the suppression of thermal excitation at low temperatures, the DCR decreases to approximately 5 mHz/mm² at $V_{\text{ov}} = 2.5$ V, which is about 7 orders of magnitude lower than at room temperature. At this point, the dark counts are primarily caused by tunneling effects, which increase exponentially with the overvoltage [15], [30].

2) *Correlated noise probability*: In a SiPM, when detecting photons, primary SPE events are generated along with the probability of optical crosstalk (direct and delayed) and afterpulses. During avalanche amplification, a SPAD may emit isotropic secondary photons. If a secondary photon escapes and enters the depletion region of another SPAD, it causes direct crosstalk, while if it initially enters a non-depleted region and later moves into the depletion region, it causes delayed crosstalk. Additionally, secondary electrons captured by impurities may later release and trigger a secondary avalanche, resulting in afterpulses.

Ref. [25], [36] describes the shapes of crosstalk and afterpulses, along with methods for their discrimination. However, at 10 mK, waveform distortion complicates this discrimination, so we analyze them collectively as correlated noises. Due to secondary avalanches, the charges associated with crosstalk or afterpulses are typically greater than those of primary signals. We set 1.5 P.E.C. as an empirical threshold to estimate occurrence probabilities: signals exceeding this threshold are considered correlated noises, while those below are regarded as primary SPE signals. The ratio of correlated noises to total signals represents the correlated noise probability (P_{cn}), which is given by

$$P_{\text{cn}} = \frac{N(> 1.5 \text{ P.E.C.})}{N(\text{total})} \quad (14)$$

where $N(> 1.5 \text{ P.E.C.})$ is the number of signals with charge exceeding 1.5 P.E.C., and $N(\text{total})$ is the total number of detected signals.

Fig. 8(a) shows the charge-amplitude distribution of 10,000 dark noise signals recorded by the oscilloscope in a dark environment at 10 mK. It can be seen that the threshold of 1.5 P.E.C. effectively separates the primary single-photon signals from the correlated noise signals. The function of P_{cn} as a function of overvoltage is shown in Fig. 8(b), increasing quadratically to approximately 18.8% at $V_{\text{ov}} = 2.5$ V. This trend highlights that while thermal background is negligible, operating voltage must be carefully optimized to manage correlated avalanches and avoid second divergence.

IV. DISCUSSION AND CONCLUSION

A. Physics of silicon avalanche at mK temperatures

The experimental results confirm that silicon PN junctions retain robust Geiger-mode avalanche multiplication capabilities down to 10 mK, answering the fundamental question posed at the outset of this study. The behavior of the breakdown voltage reveals a distinct competition between two physical mechanisms. From 100 K to 50 K, V_{bd} decreases, driven by the suppression of phonon-assisted scattering, which increases the carrier mean free path. Conversely, the anomalous increase in V_{bd} from 50 K down to 10 mK is a signature of carrier freeze-out. In this regime, the thermal ionization of dopants becomes inefficient, necessitating a higher electric field to initiate impact ionization. Despite this, the gain remains on the order of 10^6 , reduced only by a factor of ~ 4.44 compared to room temperature, which is consistent with the reduction in junction capacitance. This high intrinsic gain is a pivotal advantage over superconducting sensors that require complex SQUID readouts.

B. Noise performance and operational challenges

The most significant benefit of the 10 mK operation is the suppression of thermal noise. The measured DCR of 5 mHz/mm² represents a 7-order-of-magnitude improvement over room temperature, making the intrinsic detector noise negligible for most rare-event searches. However, challenges remain. The correlated noise (crosstalk and afterpulses) is prominent (18.8% at $V_{\text{ov}} = 2.5$ V) and increases quadratically with overvoltage, leading to a “second divergence” that limits the stable operating window to approximately 5 V. Additionally, the sharp reduction in junction capacitance at 10 mK leads to faster pulse decays, causing signal ringing and overshoot due to impedance mismatches in the coaxial cables. Future readout electronics must be specifically impedance-matched for the mK environment to fully exploit the device’s timing resolution.

C. Validation of the S-I-P-N detector concept

The successful characterization of SiPMs at 10 mK validates the semiconductor amplification stage of our proposed S-I-P-N (Superconductor-Insulator-P-N) detector. The proposed architecture, utilizing quasiparticle tunneling from a superconductor into an electron-multiplying PN junction, theoretically combines the sub-meV energy resolution of superconductors with the macroscopic readout signal of semiconductors. Unlike TES, which rely on thermal equilibrium measurements, the S-I-P-N concept detects non-equilibrium quasiparticles with high gain, offering potential advantages in pile-up rejection and particle identification.

D. Conclusion and outlook

In summary, we have demonstrated that commercial silicon avalanche devices operate reliably at 10 mK, exhibiting high gain and negligible dark counts. This finding clears the primary technical obstacle for realizing hybrid superconductor-semiconductor detectors. Future work will focus on the second phase of development: fabricating the tunnel interface

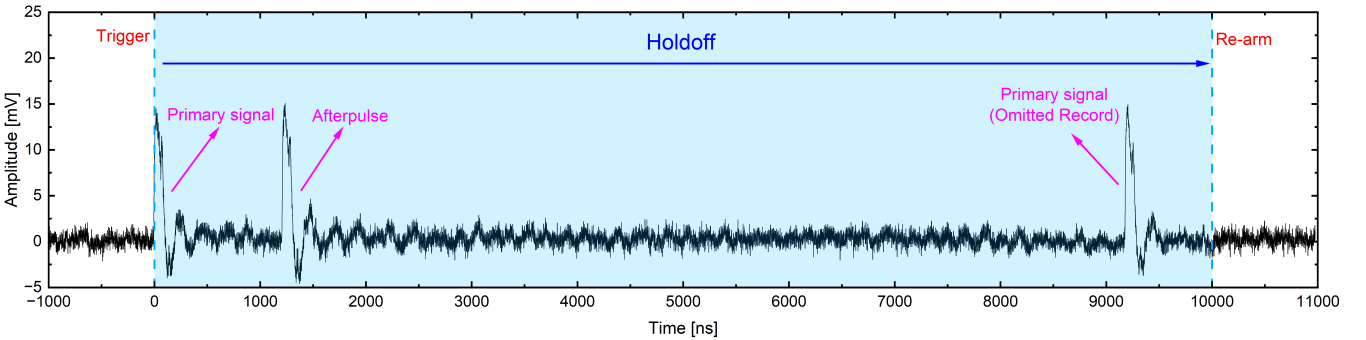


Fig. 7. A dark noise waveform with an afterpulse recorded by the oscilloscope under the self-triggering mode combined with the hold-off mode. After a dark event is triggered, the oscilloscope immediately enters a $10\ \mu\text{s}$ hold-off time, during which any subsequent afterpulses or delayed crosstalk will not be triggered. However, real dark events occurring within this period will also not be triggered, resulting in missed counts. Fortunately, the true DCR can be corrected using statistical methods.

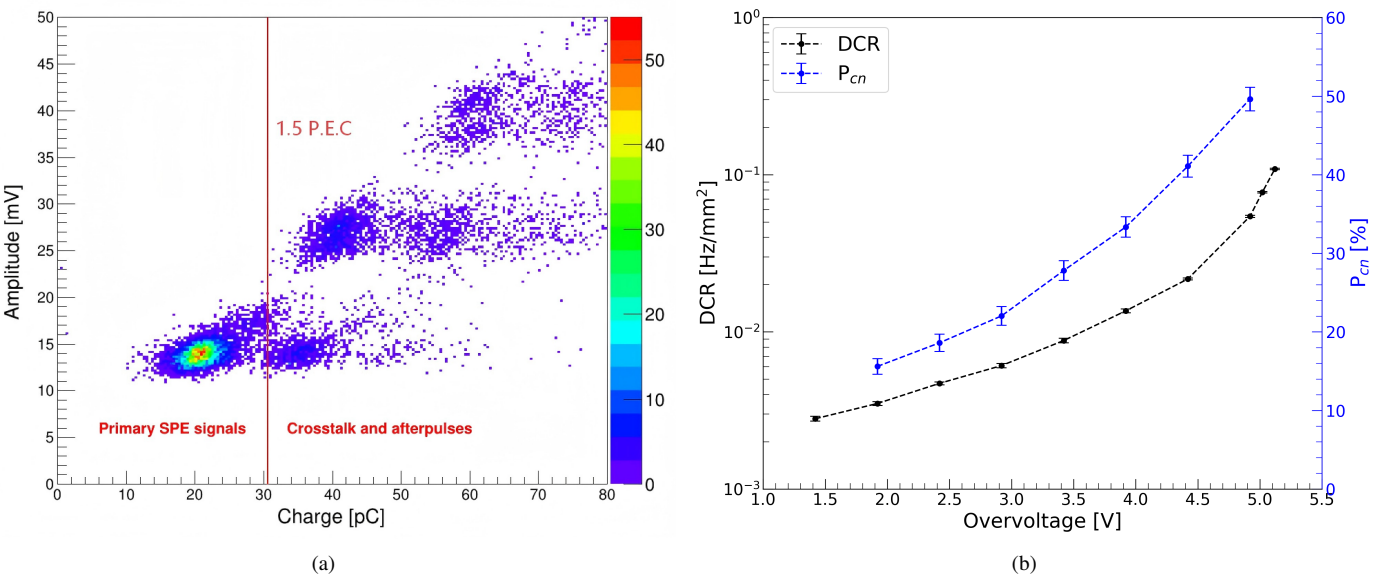


Fig. 8. (a) The distribution of dark noise charge versus amplitude at $10\ \text{mK}$. The red line indicates the position where the charge is $1.5\ \text{P.E.C.}$; signals to the left of the red line are primary single-photon signals, while those to the right are correlated noises. (b) DCR and P_{cn} as a function of overvoltage at $10\ \text{mK}$. At $V_{\text{ov}} = 2.5\ \text{V}$, the DCR is reduced to $5\ \text{mHz/mm}^2$, corresponding to a decrease of 7 orders of magnitude compared to room temperature. The error bars represent the statistical uncertainties arising from Poisson counting statistics, propagated through the dead-time correction. However, P_{cn} remains at a relatively high level, with the error being statistical.

between the superconducting absorber (e.g., Al) and the silicon multiplication layer, and evaluating the quasiparticle injection efficiency. The S-I-P-N detector represents a promising new pathway for detecting light dark matter and cosmic neutrinos, offering a scalable alternative to current quantum sensing technologies.

REFERENCES

- [1] Planck Collaboration et al., "Planck 2018 results: VI. Cosmological parameters," *A&A*, vol. 641, p. A6, Sept. 2020, doi: 10.1051/0004-6361/201833910.
- [2] M. Battaglieri et al., "US Cosmic Visions: New Ideas in Dark Matter 2017: Community Report," arXiv preprint arXiv:1707.04591, Jul. 2017. [Online]. Available: <https://doi.org/10.48550/arXiv.1707.04591>.
- [3] U. K. Dey, "Cosmic neutrino background: a minireview," *Eur. Phys. J. Spec. Top.*, vol. 233, no. 11-12, pp. 2149-2161, Oct. 2024, doi: 10.1140/epjs/s11734-024-01101-w.
- [4] M. Nenoi, "Evolution of Ionizing Radiation Research," IntechOpen, 2015. doi: 10.5772/59330.
- [5] Y. Hochberg et al., "Superconducting Detectors for Superlight Dark Matter," *Phys. Rev. Lett.*, vol. 116, no. 1, p. 011301, Jan. 2016, doi: 10.1103/PhysRevLett.116.011301.
- [6] M. D. Lucia et al., "Transition Edge Sensors: Physics and Applications," *Instruments*, vol. 8, no. 4, p. 47, Oct. 2024, doi: 10.3390/instruments8040047.
- [7] C. M. Natarajan et al., "Superconducting nanowire single-photon detectors: physics and applications," *Supercond. Sci. Technol.*, vol. 25, no. 6, p. 063001, June 2012, doi: 10.1088/0953-2048/25/6/063001.
- [8] C. Pepe, "Development of Superconducting Single-Particle Detector Transition-Edge Sensor," Ph.D. dissertation, Politecnico di Torino, Italy, 2024. [Online]. Available: <https://hdl.handle.net/11696/82079>.
- [9] K. Ramanathan et al., "Quantum Parity Detectors: a qubit based particle detection scheme with meV thresholds for rare-event searches," 2024, *arXiv:2405.17192*.
- [10] X. Li et al., "Cosmic-ray-induced correlated errors in superconducting qubit array," *Nat Commun*, vol. 16, no. 1, p. 4677, May 2025, doi: 10.1038/s41467-025-59778-z.
- [11] M. D. Shaw et al., "Quantum capacitance detector: A pair-breaking radiation detector based on the single Cooper-pair box," *Phys. Rev. B*, vol. 79, no. 14, p. 144511, Apr. 2009, doi: 10.1103/PhysRevB.79.144511.
- [12] P. M. Echternach et al., "Single photon detection of 1.5 THz radiation

with the quantum capacitance detector," *Nat Astron*, vol. 2, no. 1, pp. 90–97, Nov. 2017, doi: 10.1038/s41550-017-0294-y.

[13] J. Bardeen et al., "Theory of Superconductivity," *Phys. Rev.*, vol. 108, no. 5, pp. 1175–1204, Dec. 1957, doi: 10.1103/PhysRev.108.1175.

[14] C. R. Crowell et al., "Temperature dependence of avalanche multiplication in semiconductors," *Applied Physics Letters*, vol. 9, no. 6, pp. 242–244, Sept. 1966, doi: 10.1063/1.1754731.

[15] S.M. Sze et al., "Physics of Semiconductor Devices", John Wiley & Sons, Ltd, 2006, ISBN: 9780470068328.

[16] F. Acerbi et al., "High Efficiency, Ultra-High-Density Silicon Photomultipliers," *IEEE J. Select. Topics Quantum Electron.*, vol. 24, no. 2, pp. 1–8, Mar. 2018, doi: 10.1109/JSTQE.2017.2748927.

[17] F. Acerbi and S. Gundacker, "Understanding and simulating SiPMs," *Nuclear Instruments and Methods in Physics Research Section A: Accelerators, Spectrometers, Detectors and Associated Equipment*, vol. 926, pp. 16–35, May 2019, doi: 10.1016/j.nima.2018.11.118.

[18] P. Eckert et al., "Characterisation studies of silicon photomultipliers," *Nucl. Instrum. Methods Phys. Res. A, Accel. Spectrom. Detect. Assoc. Equip.*, vol. 620, no. 2–3, pp. 217–226, Aug. 2010, doi: 10.1016/j.nima.2010.03.169.

[19] R. Klanner, "Characterisation of SiPMs," *Nucl. Instrum. Methods Phys. Res. A, Accel. Spectrom. Detect. Assoc. Equip.*, vol. 926, pp. 36–56, May 2019, doi: 10.1016/j.nima.2018.11.083.

[20] M. Ramilli et al., "Silicon Photomultipliers: Characterization and Applications," in *Photodetectors*, S. Gateva, Ed., InTech, 2012. doi: 10.5772/36455.

[21] M. Caccia et al., "Silicon Photomultipliers and SPAD imagers in biophotonics: Advances and perspectives," *Nucl. Instrum. Methods Phys. Res. A, Accel. Spectrom. Detect. Assoc. Equip.*, vol. 926, pp. 101–117, May 2019, doi: 10.1016/j.nima.2018.10.204.

[22] Bluefors, "XLDs1 Dilution Refrigerator Measurement System," Accessed: Nov. 17, 2025. [Online]. Available: <https://bluefors.com/products/dilution-refrigerator-measurement-systems/xldsl-dilution-refrigerator-measurement-system>.

[23] *OnSemi J-Series SiPM Datasheet*, Accessed: Sep. 2023. [Online]. Available: <https://www.onsemi.cn/download/data-sheet/pdf/microj-series-d.pdf>.

[24] *LMH6629 Amplifier Datasheet*, Accessed: Aug. 2023. [Online]. Available: <https://www.ti.com/lit/ds/symlink/lmh6629.pdf>.

[25] L. Wang et al., "Characterization of VUV4 SiPM for liquid argon detector," *J. Inst.*, vol. 16, no. 07, p. P07021, July 2021, doi: 10.1088/1748-0221/16/07/P07021.

[26] A. Duara et al., "Experimental and extraction procedure for the electrical characterisation of silicon photomultiplier detectors," *Nucl. Instrum. Methods Phys. Res. A, Accel. Spectrom. Detect. Assoc. Equip.*, vol. 979, p. 164483, Nov. 2020, doi: 10.1016/j.nima.2020.164483.

[27] ROOT Team, CERN, "RooCrystalBall Class Reference," CERN ROOT Documentation. [Online]. Available: <https://root.cern.ch/doc/master/classRooCrystalBall.html>. [Accessed: Nov. 15, 2025].

[28] J. Zhang et al., "Scintillation detectors with silicon photomultiplier readout in a dilution refrigerator at temperatures down to 0.2 K," *J. Inst.*, vol. 17, no. 06, p. P06024, June 2022, doi: 10.1088/1748-0221/17/06/P06024.

[29] V. Chmill et al., "Study of the breakdown voltage of SiPMs," *Nuclear Instruments and Methods in Physics Research Section A: Accelerators, Spectrometers, Detectors and Associated Equipment*, vol. 845, pp. 56–59, Feb. 2017, doi: 10.1016/j.nima.2016.04.047.

[30] A. Gola et al., "NUV-Sensitive Silicon Photomultiplier Technologies Developed at Fondazione Bruno Kessler," *Sensors*, vol. 19, no. 2, p. 308, Jan. 2019, doi: 10.3390/s19020308.

[31] L. Darroch et al., "Measuring dark currents in multiple cryogenic SiPMs with sub-pA sensitivity using an automated IV multiplexer," *IEEE Trans. Instrum. Meas.*, vol. 74, pp. 1–11, 2025, doi: 10.1109/TIM.2025.3608348.

[32] G. Collazuol et al., "Studies of silicon photomultipliers at cryogenic temperatures," *Nucl. Instrum. Methods Phys. Res. A, Accel. Spectrom. Detect. Assoc. Equip.*, vol. 628, no. 1, pp. 389–392, Feb. 2011, doi: 10.1016/j.nima.2010.07.008.

[33] G. Collazuol et al., "Low temperature and timing properties of SiPMs," presented at the DIRC2011 Workshop, 2011. [Online]. Available: https://indico.gsi.de/event/1108/contributions/1243/attachments/1018/1314/Timing_and_low_temperature_properties_of_SiPMs.pdf

[34] T. A. Wang et al., "Characterization of two SiPM arrays from Hamamatsu and Onsemi for liquid argon detector," *Nucl. Instrum. Methods Phys. Res. A, Accel. Spectrom. Detect. Assoc. Equip.*, vol. 1053, p. 168359, Aug. 2023, doi: 10.1016/j.nima.2023.168359.

[35] F. Liu et al., "Characterization of a Mass-Produced SiPM at Liquid Nitrogen Temperature for CsI Neutrino Coherent Detectors," *Sensors*, vol. 22, no. 3, p. 1099, Jan. 2022, doi: 10.3390/s22031099.

[36] F. Acerbi et al., "Cryogenic Characterization of FBK HD Near-UV Sensitive SiPMs," *IEEE Trans. Electron Devices*, vol. 64, no. 2, pp. 521–526, Feb. 2017, doi: 10.1109/TED.2016.2641586.

[37] F. Acerbi et al., "NUV and VUV sensitive Silicon Photomultipliers technologies optimized for operation at cryogenic temperatures," *Nucl. Instrum. Methods Phys. Res. A, Accel. Spectrom. Detect. Assoc. Equip.*, vol. 1046, p. 167683, Jan. 2023, doi: 10.1016/j.nima.2022.167683.